

Rotordynamic Force Coefficients of Volute and Diffusers for Prediction of Turbomachinery Vibration

Farzam Mortazavi

Mem. ASME

Department of Mechanical Engineering,
Texas A&M University,
College Station, TX 77843
e-mail: farzam.mortazavi@tamu.edu

Alan Palazzolo

James J. Cain Professor I

Fellow ASME

Department of Mechanical Engineering,
Texas A&M University,
College Station, TX 77843
e-mail: a-palazzolo@tamu.edu

The American Petroleum Institute (API) level II vibration stability analysis for impellers requires higher fidelity models to predict the dynamic forces of the whirling impeller. These forces are in turn required to predict the vibration stability, critical speeds, and steady-state vibration response of the shaft-bearing-seal-impeller system. A transient computational fluid dynamics (CFD)-based approach is proposed which is applicable to nonaxisymmetric turbomachinery components, such as the volute and/or diffuser vanes, unlike its predecessor models like the bulk-flow or the quasi-steady model. The key element of this approach is the recent advancements in mesh deformation techniques which permit less restrictive motion boundary conditions to be imposed on the whirling impeller. The results quantify the contributions of the volute and/or the diffuser to the total forces which guides the analyst on whether to include these components in the model. The numerical results obtained by this approach are shown to agree well with experimental measurements and to be superior to the earlier quasi-steady alternative in terms of accuracy. Furthermore, several volute shapes were designed and analyzed for the sensitivity of the solution to the geometrical properties of the volute. The design flow rotordynamic forces show a significant dependence on the presence of the volutes in the model, with the specific shape of the volute having a lesser influence. The dimensionless forces are shown to be almost independent of the spin speed. [DOI: 10.1115/1.4039725]

Keywords: rotordynamics, vibration, impeller, volute, diffuser, shroud, CFD

Introduction

Anticipating possible sources of vibration and rotordynamic instability is a vital step in the design process of turbomachinery components. The geometry as well as the complex nature of the flow inside impellers and their associated components such as volutes, leakage passages, and diffuser vanes will not easily lend themselves to rotordynamic analysis. However, similar to the other turbomachinery components, at certain operating conditions, the developed dynamic forces may excite the whirling motion and lead to an undesired instability. Noting that impellers, especially pumps, regularly operate at off-design conditions, and imbalance may easily form after a duration of operation, they are prone to whirling vibration [1]. For this reason, American Petroleum Institute (API) level II stability criterion requires further analysis to account for “*all sources that contribute to the overall stability*” [2]. Among these sources, impellers have been a special concern of turbomachinery specialists [3–5]. Due to significance of the topic in power, oil, and aviation industries as well as biomedical applications [6,7], pioneering experimental studies were done to measure such forces despite significant challenges [8–10]. Dynamic forces of a shrouded impeller mainly arise from the asymmetric distribution of pressure over the impeller front shroud, which is caused by the eccentric whirling motion of impeller [11]. Theoretical models were developed to gain a deeper knowledge of the problem while reducing the time and cost needed for such analysis [12–14]. With the advent of computational fluid dynamics (CFD) and its wide application in the turbomachinery industry [15–17], several researchers [18,19] employed quasi-steady and small perturbation models to obtain the dynamic forces caused by the impeller shrouds without the major simplifications of the prior theoretical models. The quasi-steady model has been shown to

effectively predict the major portion of the dynamic forces coming from the impeller [20,21].

A quasi-steady model turns a transient problem into a steady one by solving the problem in the whirling frame [22]. A limitation of the quasi-steady and bulk-flow models compared with the transient model is that while they can be applied to nonaxisymmetric problems, these applications are approximate in the sense that some nonzero terms in the rotating frame form of the Navier–Stokes equations must be assumed to be negligible. The degree to which accuracy of the rotordynamic impedances is compromised with use of the quasi-steady model is provided by the results in this paper. Therefore, they cannot account for the impact of the volute, diffuser vanes, or impellers without a shroud (open impellers). The diffuser helps the conversion of kinetic energy to potential energy by guiding the impeller outflow through a streamlined diffusing passage. Similarly, the volute collects the discharge flow and further converts the energy downstream. This is especially becoming more relevant as the new minimum performance requirements demand addition of diffuser vanes for an efficiency boost. Several experimental and theoretical impeller rotordynamic studies have accounted for the presence of a volute or diffuser before [8,12,13,23,24]. Chamieh et al. [8] measured zero whirl frequency forces on an eccentric impeller inside a volute, and Jery continued the work by imposing a dynamic eccentricity [24]. Adkins and Brennen [12] used a theoretical approach to show the effect of the flow rate on the impeller rotordynamic coefficients inside a volute. Tsujimoto et al. [13] used a potential flow model to show the validity of the skew-symmetry assumption for an impeller whirling inside a volute. The current study proposes a transient CFD approach based on mesh deformation techniques to enable the analyst to include the nonaxisymmetric features in the CFD model and enhance the accuracy of impeller dynamic force predictions. There is no consensus on the contribution of the volute and the diffuser vanes to the overall rotordynamic forces. Most researchers believe that it is a small portion [1,20]. Although the shroud axial projection acts as a

Contributed by the Technical Committee on Vibration and Sound of ASME for publication in the JOURNAL OF VIBRATION AND ACOUSTICS. Manuscript received July 28, 2017; final manuscript received March 12, 2018; published online April 27, 2018. Assoc. Editor: Costin Untaroiu.

transferring medium for dynamic forces, the pressure and swirl ratio boundary conditions are largely dependent on upstream condition. Volute also contribute to the positive cross coupled stiffness, and usually, this contribution is larger than the direct stiffness. The cross coupled stiffness may have a significant influence on rotordynamic stability.

Since a complete pump model shows complex flow physics, a reliable CFD model can provide important quantitative results and qualitative insights to the analyst (see Supplemental CFD methods section for a brief discussion available under the “Supplemental Data” tab for this paper on the ASME Digital Collection). This is the first study to utilize a CFD method to obtain the rotordynamic coefficients of a volute or diffuser, and the approach presented uses a transient model which is not limited by the geometry. The current method’s solution has been numerically tested with eccentricities as small as 10% of the original experimental eccentricity, and the results remain the same as the case with the nominal eccentricity. The same conclusion can be made theoretically for small eccentricity ratios [25]. In other words, this method is not limited by the large eccentricities that are needed in experiments to overcome measurement uncertainties and which may exceed those in actual operation of the machine. Furthermore, the contributions of the shroud, volute, and diffuser vanes are extracted to shed light on the question of “which components dominate, and which components can be neglected, in the analysis?” A parametric study is performed to augment prior results for further investigation of the topic.

The paper is organized as follows: First, the dimensions and operating conditions from the experiments of Jery [24] and the CFTurbo [26] designed components are presented. Next, the numerical model will be discussed in detail, including boundary conditions, force extraction, and grid independency study. The methodology will be validated against experiments of Jery [24] in the Results section. That is followed by a comparison of several volute designs in terms of rotordynamic forces and the impact of having diffuser vanes. Finally, results regarding some secondary aspects such as the effect of “Gap A” (The radial gap between the impeller discharge and the diffuser, see Fig. 1), clearance profile, and spin speed will be presented. The results are then summarized.

Design Parameters and Dimensions

The experimental results from Jery [24] and Jery et al. [27] from CalTech have been employed in this study to validate the numerical approach. Jery’s pump case has been selected because

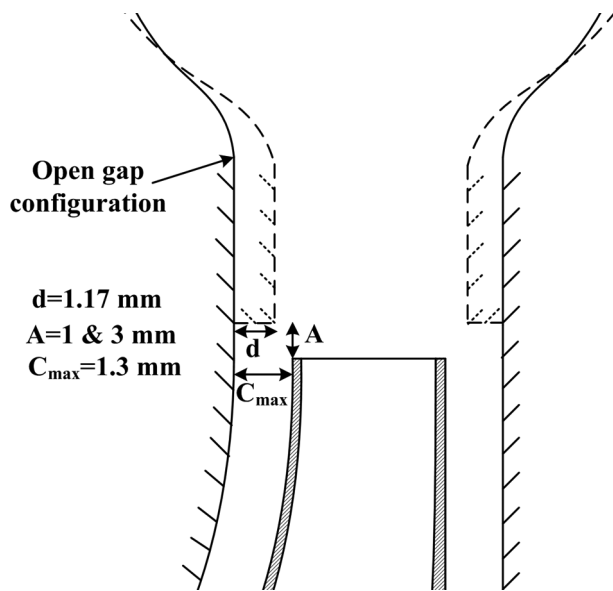


Fig. 1 Schematic of gap A configurations

more geometrical details have been discussed. Since some of the design parameters are unavailable, the commercial package CFTurbo [26] has been employed to inverse design the unknown parameters. The dimensions and the operating conditions of the pump are given in Table 1. The main dimensions are illustrated in Fig. 2(a).

Jery’s original clearance dimensions have been obtained from Ref. [12] which has a fairly large clearance. This large cavity may not be representative of today’s high performance pumps that have very tight clearances. For this reason, a second clearance has been simulated in addition to the original clearance. The second case has a tight uniform clearance profile. Both clearances are illustrated in Fig. 2(b).

In experimental measurements, sometimes the entrances of a pump side-wall gaps are temporarily sealed using flow restrictor rings in order to reduce the leakage flow. These flow restrictors artificially increase the rotordynamic forces on the impeller front shroud [12]. In the present study, such flow restrictors have been excluded to avoid unrealistically large rotordynamic forces. Also, a face seal has been included in the model to minimize the contributions of transverse fluid induced forces contributed by the seal. Other parameter of interest is the gap (gap A in Figs. 1 and 2) between the impeller discharge and the entrance of the leakage passages. A narrower gap leads to better efficiency, smoother axial thrust curves, and better stability characteristics for the head-flow curve [28]. On the other hand, it has been reported that by making this opening tighter, severe vibration problems will result [29]. Bolleter et al. [30] investigated the influence of gap A on impeller

Table 1 Dimensions and operating conditions provided by Jery [24]

Parameter	Value	Parameter	Value
β_2	23 deg	e	0.315 mm
b_2	1.58 cm	L	3.22 cm
b_3	24.75 mm	ϕ	0.092
A_{throat}	20.75 cm ²	ψ	0.49
C_r	0.13 mm	ω	1000 rpm
C_{max}	1.3 mm	Ω/ω	-1.0 to 1.0
D_0	8.0 cm	ω_s	0.57
D_2	16.2 cm	t_{sh}	3.175 mm
D_3/D_2	1.13	Z	5

The shroud thickness t_{sh} and the diffuser inlet width b_3 are found from inverse design using CFTurbo.

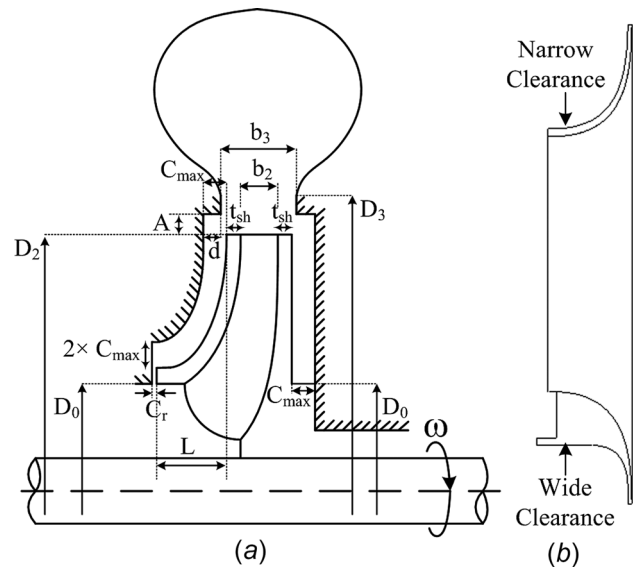


Fig. 2 Pump dimensions: (a) main dimensions and (b) narrow clearance versus wide clearance

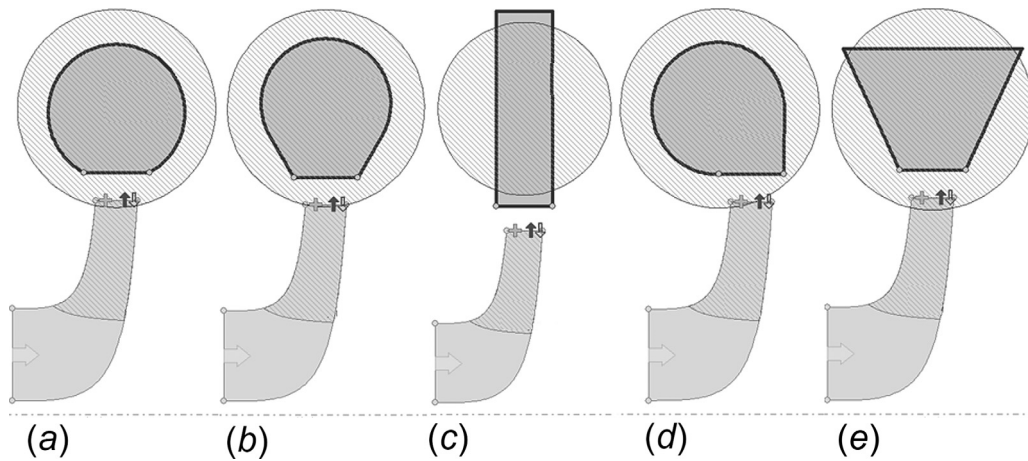


Fig. 3 Volute designs from CFTurbo: (a) circular, (b) radius based, (c) rectangular, (d) round asymmetric, and (e) trapezoidal

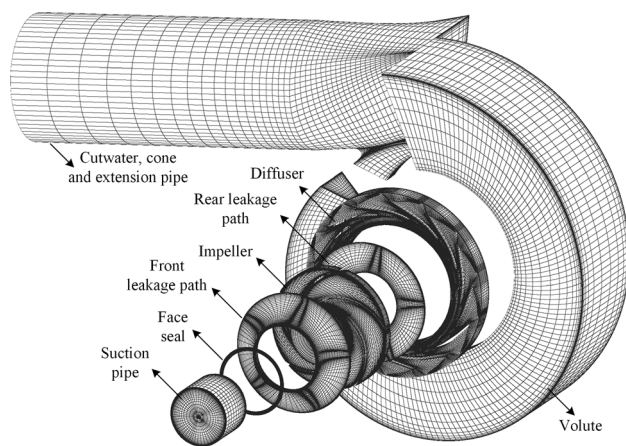


Fig. 4 Exploded view of the computational domains

rotordynamics. Accordingly, three settings of gap A have been examined, one of which completely removes the gap (see Fig. 1).

For the second part of the study, several matched flow volutes have been designed using CFTurbo, as well as a 13-vane diffuser. The number of vanes has been selected such that there is a minimum chance of resonance [31]. The volute cross sections covered in this study include trapezoidal (Trp), rectangular (Rec), circular (Cir), radius based (Rad), and round asymmetric (Rnd) designs. The vaned diffuser (Dif) has a logarithmic spiral-straight two-dimensional design. Figure 3 shows the investigated volute profiles.

Numerical Methodology

Computational Domain. All cases use a high quality fully structured grid with a maximum y^+ (the dimensionless distance from the wall defined as $y^+ = y\sqrt{\tau_w/\rho\nu}$) value of 36 for better accuracy, however, y^+ values smaller than 200 would be sufficient. Since the rotordynamic forces arise from the close interaction of the side wall gap flow with the primary flow and the diffuser/volute upstream condition, an extended model is required to include all these regions. The mesh is generated using ANSYS ICEM CFD [32,33]. The current model consists of the suction pipe, impeller, rear and front leakage paths, front face seal, diffuser vanes, volute, cutwater, discharge diffuser, and the extension pipe at the outlet. Figure 4 shows these computational domains (see Supplemental grid size section available under the “Supplemental Data” tab for this paper on the ASME Digital Collection for more details about the individual domain sizes).

Computational Fluid Dynamics Setup. The commercial CFD package ANSYS CFX 17.2 has been utilized to solve the transient Reynolds-averaged Navier-Stokes equations with the turbulence model $k - \omega$ s hear stress transport, the validity of which has been tested in numerous turbomachinery studies [34–37]. The inlet mass flow rate and the outlet static pressure boundary conditions have been imposed. All the walls use a no-slip boundary condition with a smooth wall condition. A transient rotor-stator interface has been utilized between the rotating and stationary domains. The convergence criterion for the residuals has been set to 10^{-5} .

The current study uses the mesh deformation technique to model the whirling motion of the impeller inside the casing. The displacements are imposed on boundaries as well as subdomains to reduce total computational cost and improve mesh quality. A diffusion equation for the mesh has to be solved at each time-step [38] in order to diffuse the imposed motions on the boundary nodes to the interior nodes. The diffusion equation is solved to reach a residual value of 10^{-5}

$$\nabla \cdot (\Gamma_\delta \nabla \delta) = 0 \tag{1}$$

where the displacement relative to the previous location of the node has been shown with the symbol δ , and Γ_δ denotes the mesh stiffness. By expressing the mesh stiffness in terms of cell volume, one can shift the deformation area to the regions with coarser mesh (far from the walls), and in this way, preserve the orthogonality of the grid adjacent to the wall

$$\Gamma_\delta = \left(\frac{V_{\text{ref}}}{V} \right)^{C_{\text{stiff}}} \tag{2}$$

The reference volume V_{ref} is set to the mean cell volume size in the grid, and the stiffness exponent C_{stiff} has been set to 2.0 in this work. By imposing boundary conditions in the Laplace equation, one can preserve the boundary original shape as well as its normal derivative which improves the mesh orthogonality near the walls [39]. The avid reader is encouraged to refer to the ANSYS CFX theory guide [38] for further details. The mesh deformation boundary conditions are shown in Fig. 5 considering both the blade to blade and meridional views. In this work, a subdomain has been defined which contains the impeller. Since all the nodes inside the subdomain have the same whirling displacement, the cells will not be deformed with respect to each other; hence, the mesh quality inside the impeller is preserved. The deformation happens in a region far from the impeller called the absorption domain. Both the subdomain and the absorption domain are parts of an assembly domain which has the rotational speed of the spinning motion.

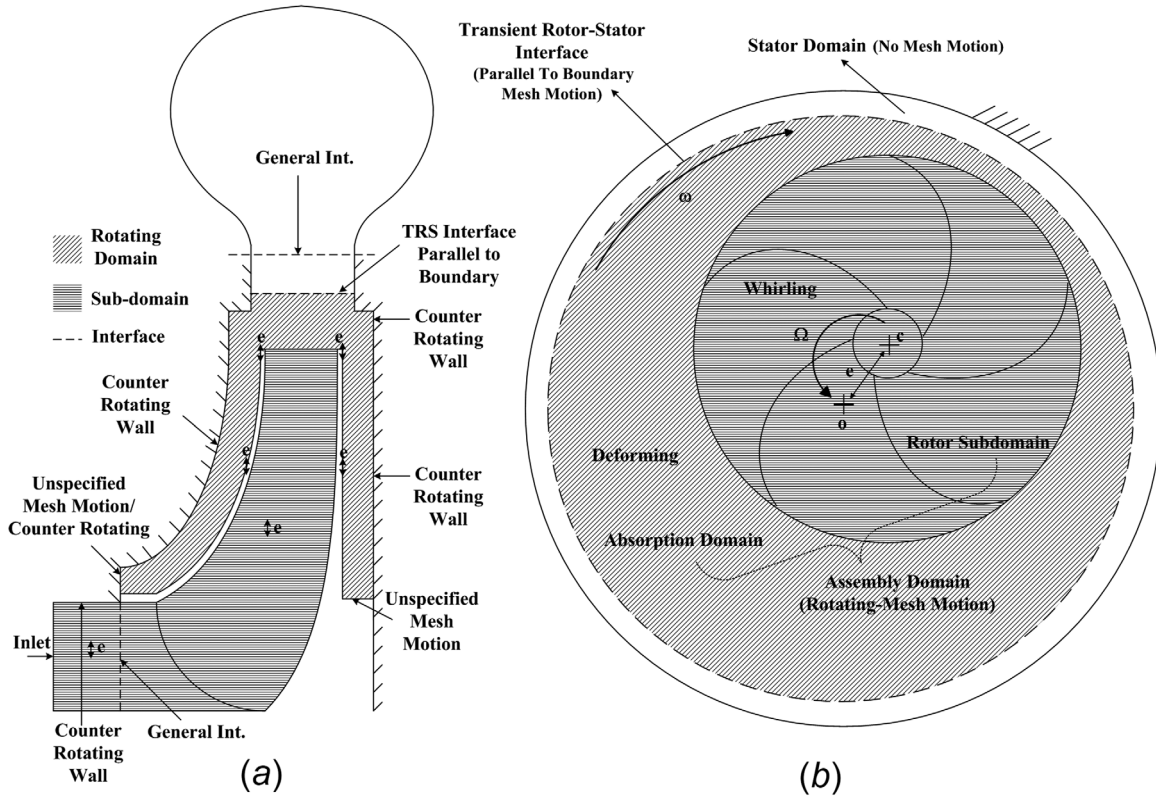


Fig. 5 Mesh deformation boundary conditions: (a) blade to blade view and (b) meridional view

The circular whirling motion is imposed by introducing a ramp function to avoid rapid mesh distortion

$$e_x = e \cos \omega t \mathbb{H}\left(|\omega|t - \frac{\pi}{2}\right) \quad (3)$$

$$e_y = e \sin \omega t$$

Force Extraction Method. The transient stationary frame force results are collected after allowing the solution to reach its periodic state. At least ten spinning cycles are simulated for each case. There are a number of forces present in this simulation, each of them having its own frequency such as the blade pass peak, spin peak, whirl peak, and higher harmonic. Figure 6 shows an example of the frequency peaks present in this study. For instance, the blade pass peak appears at the frequency ratios $Z_b \pm 1$ as it modulates with the single vane volute (the tongue). However, there is only interest in the whirl frequency peak in accordance to the rotordynamic vibrations motivations of this study. To this end, a Fourier transform will be applied to the stationary frame forces to extract the whirl component.

The amplitude and phase angles of the whirling component have been used to reconstruct the normal and tangential forces in the whirling frame. Thus, the impedance curves have been obtained. Subsequently, a root-mean-square (RMS) second-order curve fitting has been performed to obtain the dynamic coefficients. Owing to the skew symmetry of the rotordynamic force coefficient matrices [24], one set of direct and cross-coupled dynamic coefficients for stiffness, damping, and inertia terms will be sufficient. The applicability of the skew-symmetry assumption has been previously validated by the prior theoretical and experimental works in the area of impeller rotordynamic forces [12,13,24] which have accounted for transient effects.

All the results in this study have been delivered in dimensionless format to promote comparability and their range of applicability. The dimensionless forces are defined as

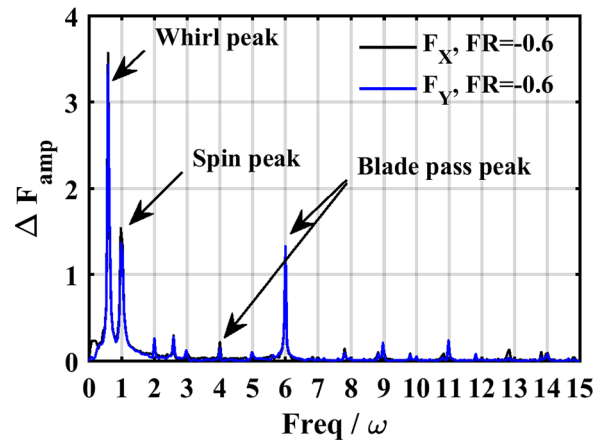


Fig. 6 Sample fast Fourier transform (FFT) of the dimensionless forces in the stationary frame at $FR = -0.6$

$$F_N = \frac{f_n}{\rho \pi r_2^2 \omega^2 b_2 e}, \quad F_T = \frac{f_t}{\rho \pi r_2^2 \omega^2 b_2 e} \quad (4)$$

Similarly, the dimensionless rotordynamic coefficients are defined as follows. The coefficients are defined in the Nomenclature and the symbols shown with “^” represent the dimensional values

$$\mathcal{K} = \frac{\hat{K}}{\rho \pi r_2^2 \omega^2 b_2}, \quad \ell = \frac{\hat{k}}{\rho \pi r_2^2 \omega^2 b_2}$$

$$\mathcal{C} = \frac{\hat{C}}{\rho \pi r_2^2 \omega b_2}, \quad c = \frac{\hat{c}}{\rho \pi r_2^2 \omega b_2} \quad (5)$$

$$\mathcal{M} = \frac{\hat{M}}{\rho \pi r_2^2 b_2}, \quad m = \frac{\hat{m}}{\rho \pi r_2^2 b_2}$$

which are determined from the numerically calculated impedances, fitted to the standard quadratic form model

$$\begin{bmatrix} F_N \\ F_T \end{bmatrix} = \begin{bmatrix} -\mathcal{K} - c \frac{\Omega}{\omega} + \mathcal{M} \frac{\Omega^2}{\omega^2} \\ k - \mathcal{C} \frac{\Omega}{\omega} - m \frac{\Omega^2}{\omega^2} \end{bmatrix} \quad (6)$$

The dimensionless rotordynamic coefficients are found by using a least square curve fitting method. Impellers are known to show deviations from a second-order curve fitting approach, requiring instead a more general transfer function model. Previously, attempts have been made by several scholars to use other methods than the least square curve fitting to improve the rotordynamic coefficients of an impeller [11,12,40]. However, in terms of practicality for industrial applications, the least square curve fitting model seems to be a more attractive option.

The zero frequency ratio results ($\Omega/\omega = 0$) require a special treatment in the transient analysis. The circumferential averaging approach previously used by Suzuki et al. [7] has been adopted in this study to find the nonwhirling results. Figure 7 illustrates the impeller position phase model employed in this approach

$$\begin{aligned} \overline{F_N}^{\Omega=0} &= \frac{F_N^0 + F_N^{\frac{\pi}{2}} + F_N^{\pi} + F_N^{\frac{3\pi}{2}}}{4} - F_{0,N} \\ \overline{F_T}^{\Omega=0} &= \frac{F_T^0 + F_T^{\frac{\pi}{2}} + F_T^{\pi} + F_T^{\frac{3\pi}{2}}}{4} - F_{0,T} \end{aligned} \quad (7)$$

In addition, the force results at $FR = \pm 1$ have the same frequency as the spin component, thereby making them prone to uncertainty. This is especially true at $FR = 1$ where the whirling forces may be comparable in magnitude to the spinning related forces. For this reason, the results at these points have been omitted, and instead the closest points at $FR = \pm 0.9$ have been simulated and included.

Shroud, Diffuser, and Volute Force Extraction. To specify the contribution of each component to the overall dynamic forces, separate models have been devised and then subtracted from the full model that includes the entire assembly (For further details

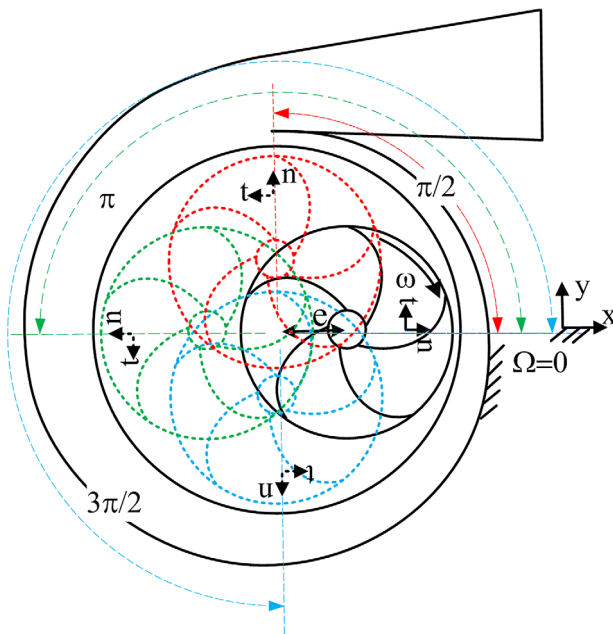


Fig. 7 Zero frequency ratio force extraction

about this procedure refer to Supplemental shroud forces section available under the “Supplemental Data” tab for this paper on the ASME Digital Collection).

Special care has been taken to remove the effects of rotating or stationary stall from simulations, especially in the case of the diffuser vanes (see Supplemental rotating stall section available under the “Supplemental Data” tab for this paper on the ASME Digital Collection). If a nonmatched diffuser is used in the simulations, the diffuser dynamic force results will be contaminated by the extra impact of flow coefficient. Impellers are typically designed to operate at their maximum efficiency which occurs at a certain flow rate known as the best efficiency point (BEP). Here, the goal is to obtain the dynamic coefficients at the best efficiency point to omit cases with an off-design operation.

Model Error. The subdomain center of spin is fixed on the initial spot (the center of spin is not whirling with the impeller). This results from the current limitations in defining the rotating frame axis of rotation as a function of time in ANSYS CFX. It will be shown that the error associated with this model will be small provided that the eccentricity ratio to the outer diameter e/D_2 is not too large which is the case in the current model.

Consider an impeller which is spinning about an off-centered axis as shown in Fig. 8. In this configuration, the velocity magnitude and, therefore, static pressure distribution on the opposite sides of the impeller will not be the same. Therefore, a resultant radial force will be formed which is not physical but instead an artifact of the fixed center of spin limitation. A quick integration over the impeller front shroud estimates the order of magnitude of this force

$$\Delta F_{N, fsh} = \frac{2 \int_{\theta=-\pi/2}^{\theta=\pi/2} \int_{r=r_0}^{r=r_2} \int_{\phi=0}^{\phi=\pi/2} \frac{1}{2} \rho (e\omega)^2 \cos \theta / \sin \phi r dr d\theta d\phi}{\pi \rho r_2^2 \omega^2 b_2 e} \quad (8)$$

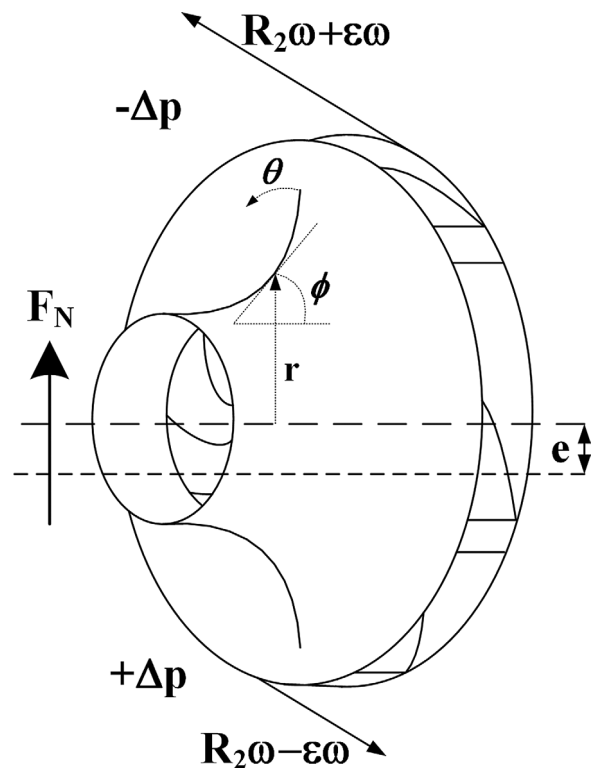


Fig. 8 Fictitious force due to the fixed axis of spin

The hub and shroud contributions almost cancel each other. It is difficult to estimate the contribution of blades due to their three-dimensional (3D) complex profile, but their contribution should be smaller or in the order of the front shroud (the blades also contribute to tangential forces). The majority of rotordynamic forces in a closed 3D centrifugal pump impeller comes from the front shroud as it has been shown in several prior studies [21,23,41–43]. This fictitious force is not a function of the whirl speed Ω , but its dimensionless magnitude depends on e ; hence, for the smaller whirl orbits, this error will be linearly reduced. Simplification of Eq. (8) and division by the total dimensionless normal force yield

$$\frac{\Delta F_{N, fsh}}{F_N} = \frac{B}{f_n}, \quad B = 2\pi D_0 L \rho (e\omega)^2 \quad (9)$$

where D_0 and L represent the impeller eye diameter and front shroud axial length, respectively. This result shows that the ratio will be negligible as long as the eccentricity and spin speed are small (which is the case in this problem). An impeller without a diffuser and volute is selected and simulated using the quasi-steady method, in order to further quantify this error term. Two eccentric cases are simulated, the first with centered and the second with off-centered spinning. The difference between the two cases quantifies the error. Jerry's original eccentricity of $e = 1.26$ mm has been imposed in both cases to present a very conservative extreme case with regard to the error estimation. The remaining simulations are more representative of actual impeller whirl magnitudes, with 25% of the original eccentricity, and therefore, the dimensionless error forces will be much smaller relative to the total forces for these cases. Figure 9 compares the two cases and shows that this error term is negligible even when using the largest eccentricity.

Grid Independency. A grid study was performed to demonstrate the independency of the results from the mesh resolution (see Supplemental grid refinement section available under the "Supplemental Data" tab for this paper on the ASME Digital Collection). Three different sets of quantities are monitored to qualitatively show that the grid convergence error is minimal [44]. The three quantities include: (1) pump head coefficient ψ , (2) pump efficiency η , and (3) the RMS of absolute dynamic force difference over a range of frequency ratios. The first quantity is indicative of the convergence of the pressure field and continuity equation. The second quantity is indicative of the resolution of boundary layers and prediction of shear stress on walls which typically requires more refined grids. The third parameter is the rotordynamic parameter of interest specific to the problem which is the

dynamic force in an average sense. This quantity cannot be defined using a single frequency ratio like the other two, so the RMS value of the difference with respect to the finest grid will be assessed

$$\text{RMS}_{\bar{F}_N} = \sqrt{\frac{\sum_{i=1}^{N_{FR}} (\bar{F}_N^{\text{finer}} - \bar{F}_N^{\text{grid}})^2}{N_{FR}}} \quad (10)$$

$$\text{RMS}_{\bar{F}_T} = \sqrt{\frac{\sum_{i=1}^{N_{FR}} (\bar{F}_T^{\text{finer}} - \bar{F}_T^{\text{grid}})^2}{N_{FR}}}$$

where N_{FR} defines the number of frequency ratios considered. Figure 10 shows the grid convergence results. According to this plot, the fine mesh (1.867×10^6 nodes) has been selected as the appropriate grid since the grid convergence parameters are almost saturated at this point, and the changes are below 5%. Figure 11 illustrates how the dynamic forces from all the grids almost fall on the same curve. Therefore, one can rely on the coarse grid results if only the dynamic coefficients are sought. This observation reduces the computational cost of the transient solution considerably. The major difference between the impeller and the seal case associates to the range of Re number. Inside the liquid annular seals, the Re number is in order of 10^4 and sometimes as low as 10^3 while in the front leakage path of the impeller, the Re

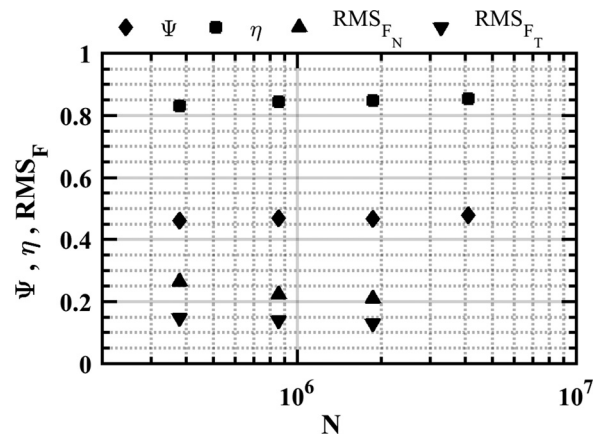


Fig. 10 Grid independency results

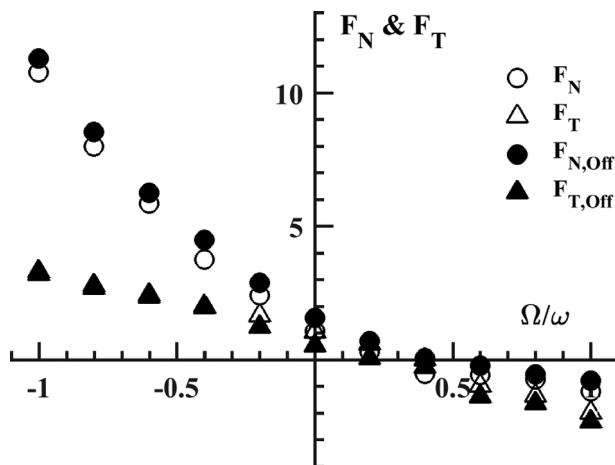


Fig. 9 Quasi-steady dimensionless normal and tangential forces with centered and off-centered spinning motion (eccentricity $e = 1.26$ mm)

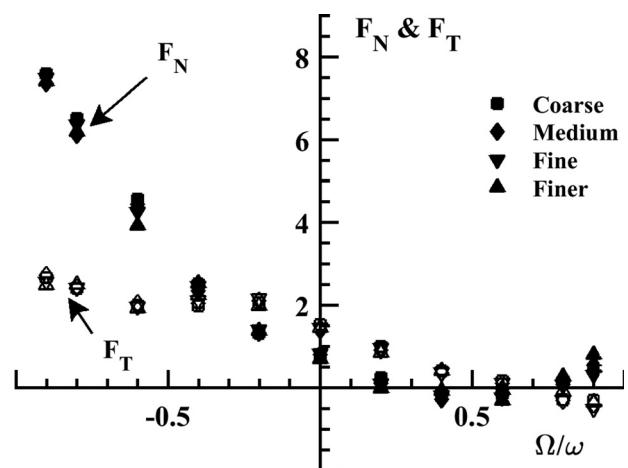


Fig. 11 Dimensionless dynamic forces from various grid densities

number is in order of 10^5 , making the utilization of wall-functions and coarse meshes more viable.

Results and Discussion

Validation. The concentric case model was compared with the characteristic measurements by Jery [24]. The numerical characteristics show the same trend as the experimental data. Figure 12 compares the numerical results against experimental values for the head coefficient and the efficiency.

For the whirling case, the measurements from Jery have been compared to the numerical results from both the quasi-steady model and the transient model (see Fig. 13). These results refer to the original trapezoidal volute without diffuser vanes which is called Volute A in Jery's work. Also, the clearance profile has been set to the original wide configuration in order to comply with the test geometry. The superiority of the transient method to the quasi-steady approach clearly manifests itself in these plots. Although one expects that the transient solution will provide more accurate results than the quasi-steady model, the matter of degree of improvement is of strong importance to justify the increased computational time that accompanies the transient approach. Earlier, non-CFD theoretical models have emphasized on transient effects which are absent in the quasi-steady models [13,45]. The deviation in the numerical results is primarily attributed to the uncertainties in the front shroud curve. Furthermore, the effects of

Reynolds-averaged Navier-Stokes turbulence modeling, special and temporal numerical errors, unknown surface roughness, and the duration of numerical sampling contribute to the model deviation. The quasi-steady model particularly shows more deviation because of transient effects and non-axisymmetric features. The quasi-steady predictions are much closer to the transient predictions if a narrow clearance profile is used where there is a reduction in the contribution of the volute. The results of clearance profile are presented later in the paper.

Table 2 compares the rotordynamic coefficients from the transient simulation to the experimental values. Overall, there is a reasonable agreement between all coefficients. The quasi-steady model coefficients are clearly unreliable in this case, as indicated by the results in Fig. 13.

To quantify the contribution of the volute in this case, the total forces have been subtracted from the impeller forces (without volute) and the outcome represents the volute contribution. Figure 14 compares the forces associated with the volute against the impeller forces. The normal contribution is relatively small while the tangential contribution accounts for a bigger share of the total tangential force.

Volute and Diffuser Rotordynamic Forces. The prior section's validation of the model allows the methodology to be used to explore the rotordynamic behavior of the volute and the diffuser. The five different volute designs and the vaned diffuser have been simulated with the narrow leakage path clearance configuration at the design flow rate, since it is sought to show that the volute and the diffuser have a significant influence on the impedances and dynamic coefficients even for the case that the clearance is similar to the values used in those cases in the literature that exclude the diffuser and volute from their models. This will let the analyst know that if the volute and/or diffuser should be kept in the analysis or not. Also, the narrow clearance may be more practical in the actual applications. Figure 15 presents the total normal and tangential forces exerted on the same impeller operating with various volutes. Except for the rectangular volute, all the volutes follow the same curve, implying that the shape of the volute does not alter the rotordynamic coefficients at the BEP.

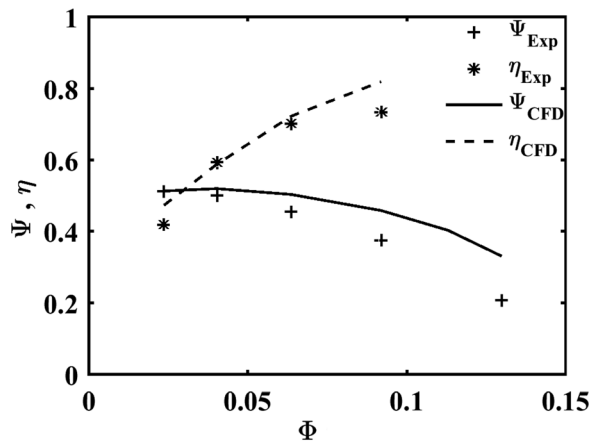


Fig. 12 Experimental and numerical pump characteristics

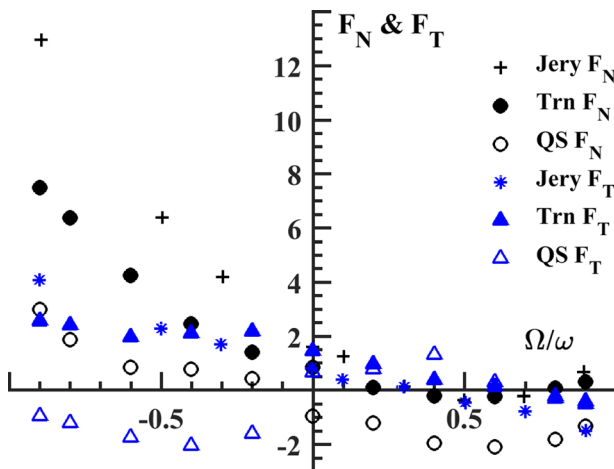


Fig. 13 Dimensionless normal and tangential forces, predictions versus experiments. QS and Trn correspond to quasi-steady and transient, respectively.

Table 2 Experimental versus CFD predicted rotordynamic coefficients

Case	\mathcal{K}	\mathcal{L}	\mathcal{C}	c	\mathcal{M}	m
Jery	-1.64	0.82	2.94	6.88	6.39	-0.64
CFD	-0.85	1.44	1.74	3.86	4.05	0.59
Rel. Error (%)	48.2	75.6	40.8	43.9	36.6	192

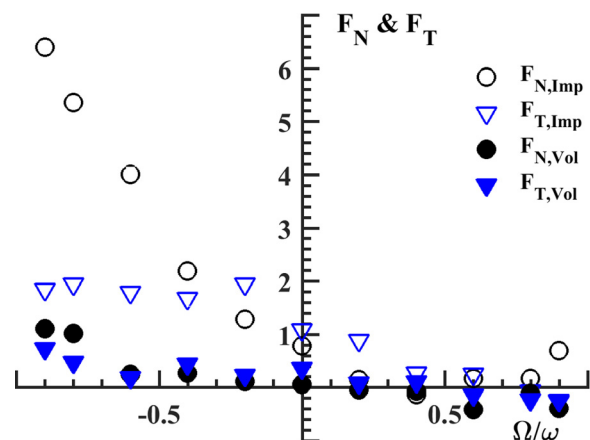


Fig. 14 The trapezoidal volute rotordynamic forces versus the impeller for the wide clearance configuration

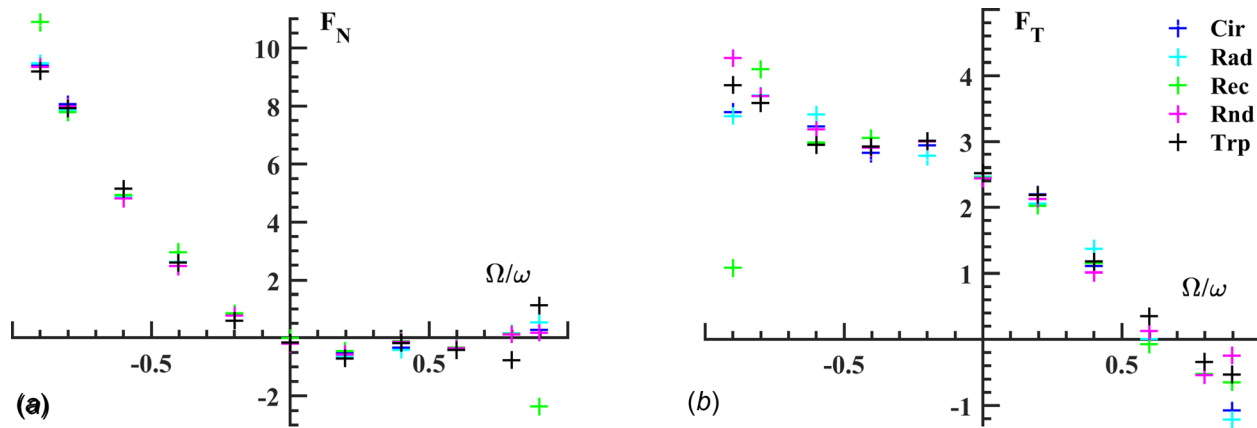


Fig. 15 Total dimensionless normal and tangential forces of the same impeller working with various volutes

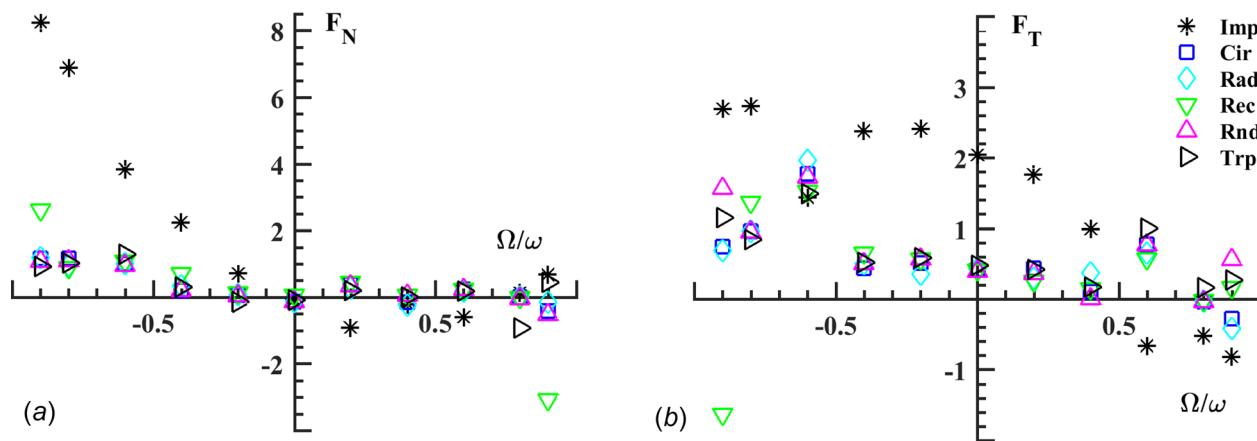


Fig. 16 Contributions of the impeller and various volutes to the total normal and tangential forces

Note that a nonmatched volute introduces the effects of the flow rate coefficient which contaminates the results and, therefore, has been avoided. Also, the rectangular volute shows an uncommon sudden drop of the tangential force at $FR = -0.9$ which has a destabilizing effect.

To better visualize the contribution of the volutes, the dynamic forces has been subtracted from the transient solution of the impeller forces alone (no volute) which serve as the base line forces. As was shown before, the quasi-steady model cannot serve as the base line due to its axisymmetric assumption. Although not shown here, the quasi-steady base line erroneously overpredicts the contribution of the diffuser and the volute. Figure 16 shows that at certain frequency ratios, the volutes contribute comparable forces as the impeller. The introduction of the volutes has shifted the whirl frequency ratio (WFR) from 0.5 (see Fig. 16(b)) to 0.65 (see Fig. 15(b)). Table 3 does a basic comparison between the dimensionless dynamic coefficients of the impeller and the volutes. According to Table 3, all the volutes have a comparable

direct stiffness with respect to the impeller. The volutes show about 25% of the impeller cross coupled stiffness. Furthermore, the volutes provide a direct damping close to 30% of the impeller direct damping (with the exception of the rectangular volute). However, the volute impedances are nonquadratic and their impact is better represented by the rotordynamic forces rather than the rotordynamic coefficients. The effect of nonquadratic curves on the rotordynamic stability can be further investigated using the approach introduced by Kim and Palazzolo [40].

The diffuser vanes may be integrated with a volute or be used alone with cross overs. Thus, there is an interest in both cases. Figure 17 exhibits the contributing normal and tangential forces of the diffuser vanes. In this figure, the diffuser and volute forces have been subtracted from the impeller base line forces to quantify the contribution of each component. Table 4 indicates the rotordynamic coefficients from each component. The tangential forces show more dependency on the presence of the volute or the diffuser compared to the normal forces. The diffuser has a more pronounced influence over the direct damping and the direct added mass, while the volute has a greater share in the total direct stiffness. Both components drive the forward whirl especially at larger frequency ratios, yet they have a stabilizing effect in the backward whirl region.

Table 3 Impeller and volute rotordynamic coefficients

Case	\mathcal{K}	\mathcal{L}	\mathcal{C}	c	\mathcal{M}	m
Imp	0.17	1.83	1.92	4.03	5.69	1.39
Cir	0.11	0.58	0.61	0.71	0.95	0.12
Rad	0.11	0.6	0.65	0.66	0.99	0.19
Rec	0.11	0.7	0.08	1.62	0.53	0.89
Rnd	0.11	0.44	0.62	0.69	0.87	-0.64
Trp	0.15	0.54	0.44	0.67	0.63	0.99

Impact of Clearance, Gap A, and Spin Speed. As was pointed out in the validation section, the clearance profile plays a role in deciding whether a quasi-steady model is applicable. Observe in Fig. 18 that quasi-steady predictions for the narrow clearance have a better agreement to the transient results compared to what was shown in Fig. 13 for a wide clearance. However, it should be

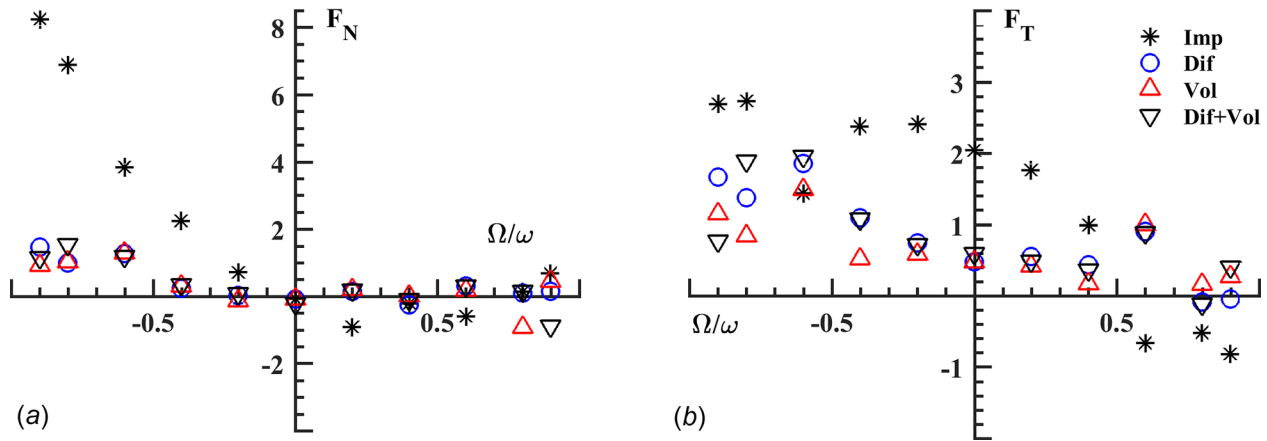


Fig. 17 Contributions of the diffuser and the volute to the total normal and tangential forces

Table 4 Comparison of impeller, diffuser, and volute rotordynamic coefficients

Case	\mathcal{K}	ℓ	\mathcal{C}	c	\mathcal{M}	m
Imp	0.17	1.83	1.92	4.03	5.69	1.39
Dif	0.06	0.50	0.89	0.66	1.18	-0.59
Vol	0.15	0.54	0.44	0.67	0.63	0.99
Dif + Vol	0.21	0.60	0.72	0.90	1.13	-0.41

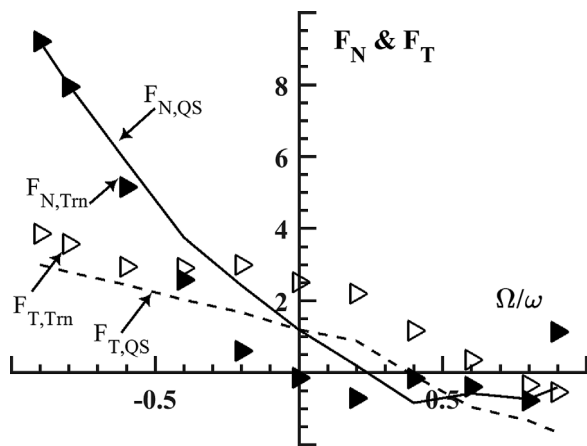


Fig. 18 The quasi-steady model predictions follow the transient results closely for the narrow clearance configuration. Trapezoidal volute is included in both cases.

pointed out that there still is a significant difference between the stiffness predictions and the resultant WFR. Figure 19 displays further detail about the influence of the clearance profile. Both configurations use a trapezoidal volute and results have been acquired by the transient model. The immediate observation is that both cases have comparable forces at the subsynchronous range of the frequency ratio. Table 5 compares the rotordynamic coefficients. The narrow clearance case has a larger cross-coupled and direct (positive) stiffness as well as direct damping, with an overall larger WFR.

The influence of gap A shown in Fig. 1 is revealed by considering the vertical intercept of the tangential forces in Fig. 20. The cross-coupled stiffness increases significantly by reducing gap A. Reduction of gap A in effect makes it behave similar to a plain annular seal, which is reflected in the trend of the rotordynamic coefficient in Table 6. Overall, the increased WFR of the tight

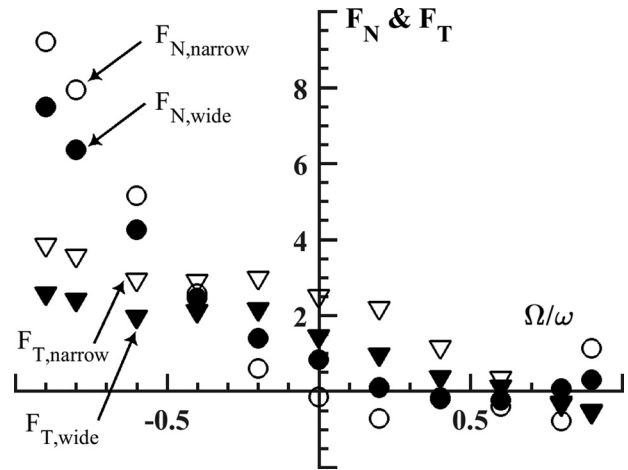


Fig. 19 Transient force predictions of the narrow versus wide clearance. Trapezoidal volute is included in both cases.

Table 5 Impact of the clearance profile on the rotordynamic coefficients

Clearance	\mathcal{K}	ℓ	\mathcal{C}	c	\mathcal{M}	m	WFR
Narrow	0.32	2.29	2.35	4.65	6.68	0.98	0.65
Wide	-0.85	1.44	1.74	3.86	4.05	-0.59	0.6

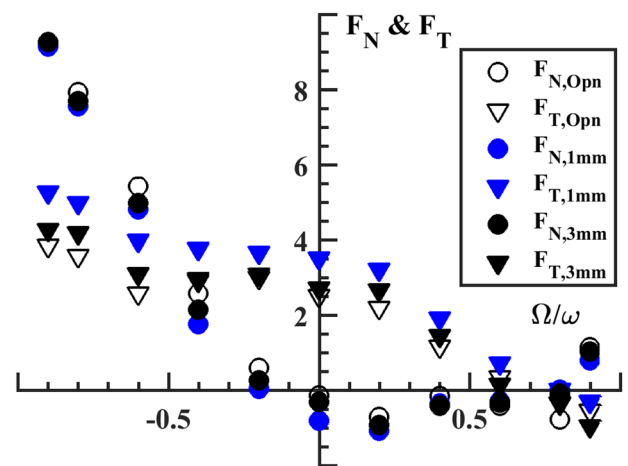


Fig. 20 Gap A influence on the dynamic forces

Table 6 Impact of the Gap A on the rotordynamic coefficients

Gap A	\mathcal{K}	ℓ	\mathcal{C}	c	\mathcal{M}	m	WFR
Open	0.04	2.36	2.31	4.74	6.27	1.13	0.65
3 mm	0.34	2.60	2.68	4.50	6.77	1.29	0.6
1 mm	0.57	3.23	2.93	4.40	6.98	1.17	0.8

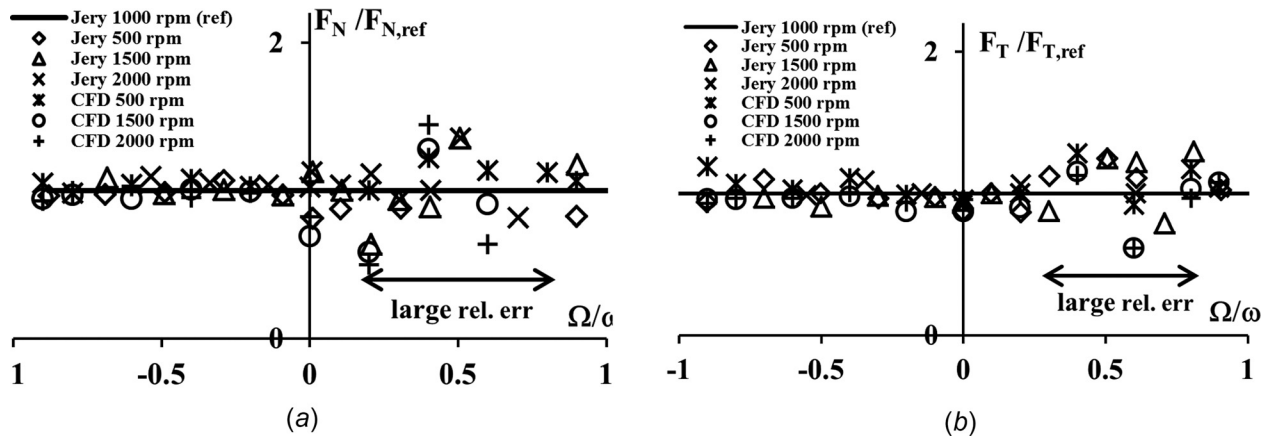


Fig. 21 Independence of the dimensionless normal and tangential forces from the spin speed

Gap A configuration ($Gap_A/D_2 = 0.006$) suggest a less favorable stability condition.

Jery [24] reported that the dimensionless dynamic forces do not show a significant dependence on spin speed. This conclusion could have a major impact on the reduction of influential variables of the problem, therefore, it was investigated by numerical means in the present work. Results from four (4) distinct spin speeds were obtained and renormalized by the reference speed forces at $\omega = 1000$ rpm ($F_N/F_{N,ref}$ and $F_T/F_{T,ref}$). Then, all the points should approach unity if the spin speed does not affect the dynamic forces. The numerical and experimental results illustrated in Fig. 21 confirm this observation. Points close to the region where F_N and F_T approach zero (for example, in Fig. 20 close to $\Omega/\omega = 0.4 - 0.8$) have higher relative error and uncertainty, and therefore, not plotted in Fig. 21. These results show that the dimensionless rotordynamic coefficients are nearly independent of spin speed, unlike the dimensional ones.

Conclusion

A CFD-based, transient methodology was presented to improve rotordynamic force coefficient predictions of impellers under more general conditions where nonaxisymmetric components such as volutes or diffusers are present. The proposed approach was shown to considerably improve the predictions compared to the quasi-steady model when the clearance profile grows wider. The grid independency study suggests that even coarse grids can be effectively used to extract the rotordynamic coefficients, provided that vibration and rotordynamic stability are the main goals of the simulation.

The relative contribution of the volute and/or diffuser to the overall dynamic forces depends on the frequency ratio and the front leakage path profile, where flow rate effects are not considered in this work. The cross-coupled stiffness from the volutes or the diffuser investigated in this study was calculated to be about 20–30% of the impeller cross coupling. The current impedance curves suggest that the presence of the diffuser or the volute increases the WFR by 0.1–0.15, which shows the destabilizing effect of these components. Furthermore, based on several volute

design trials, it was concluded that at the design point, the difference in the volute cross-sectional profile shape is immaterial while its presence has to be considered. The rectangular volute, however, showed an erratic behavior at $FR = \pm 0.9$.

A parameter study showed that by tightening gap A, which is a common practice for increasing efficiency, the cross-coupled stiffness increased significantly. Results imply that gap A effectively acts similar to a plain annular seal relative to the dynamic force coefficients. Moreover, the forces from the narrow and wide clearance profile have comparable sizes in the subsynchronous region. Spin speed shows little influence on the dimensionless rotordynamic forces, but may influence the dimensional ones.

The focus of the current study was developing the novel methodology and demonstrating its application only at the design flow rate. Interesting results may be achieved by extending the method to investigate off-design operation and/or more complex geometries such as an open impeller where conventional methods fail to predict the dynamic forces. The methodology can be further developed to attain alternative formula to the well-known Wachel and Von Nimitz [46] relation. A limitation of the current study was the unknown front shroud profile of the impeller which had to be inverse-designed. To further validate the current model, it is recommended to run calculations on an impeller with a known front shroud profile and compare the results to experiments. It is also encouraged to utilize higher fidelity turbulence models as the computational horizons expand in near future.

Acknowledgment

The authors would like to thank CFTurbo in the website link¹ for providing the inverse design tools. Portions of this research were conducted with the advanced computing resources provided by Texas A&M High Performance Research Computing.² This project was funded by the Turbomachinery Research Consortium (TRC)³ at Texas A&M University. The authors would like to

¹<http://en.cfturbo.com/>

²<https://hprc.tamu.edu/>

³<http://turbolab.tamu.edu/trc/>

express their gratitude to TRC member companies for their continued support.

Nomenclature

A_{throat} = volute throat cross section area, m^2
 b_2 = blade outlet width, m
 \hat{c}, \hat{C} = cross-coupled and direct damping coefficients, N s/m
 c, C = dimensionless cross-coupled and direct damping coefficients
 C_r = radial clearance, m
 C_{stiff} = grid stiffness exponent
 d = gap A axial length, m
 D_0, D_1, D_2, D_3 = diameter (suction, inlet, outlet and diffuser), m
 f_N, f_T = normal and tangential whirling forces, N
 f_x, f_y = whirling forces in the stationary frame, N
 F_N, F_T = dimensionless normal and tangential whirling forces
 $\overline{F_N}, \overline{F_T}$ = dimensionless normal and tangential whirling forces at FR = 0.0
 F_X, F_Y = dimensionless whirling forces in the stationary frame
 $F_{0,n}, F_{0,t}$ = dimensionless normal and tangential forces in the centered position
 g = gravitational acceleration, m/s^2
 H = pump head, m
 \mathbb{H} = step function
 \hat{k}, \hat{K} = cross-coupled and direct stiffness coefficients, N/m
 k, K = dimensionless cross-coupled and direct stiffness coefficients
 L = front shroud projected length, m
 \hat{m}, \hat{M} = cross-coupled and direct added mass coefficient, kg
 m, M = dimensionless cross-coupled and direct added mass coefficients
 N = grid size
 N_{FR} = number of frequency ratios
 p = pressure, Pa
 Q = flow rate, m^3/s
 Q_l = leakage flow rate, m^3/s
 r_0, r_2 = impeller suction and discharge radii, m
 Re = Reynolds number
 t = time, s
 t_{sh} = shroud thickness, m
 T = torque, Nm
 y = distance from the wall, m
 y^+ = solver Yplus; $y^+ = (y/\nu)\sqrt{(\tau_w/\rho)}$
 Z, Z_b = number of blades
 Z_v = number of diffuser vanes
 \forall, \forall_{ref} = cell volume, cell reference volume, m^3

Greek Symbols

e = eccentricity, m
 β_2 = blade trailing edge angle, deg
 δ = displacement, m
 η = efficiency, $(\rho g H Q)$
 θ = circumferential position, rad
 ν = kinematic viscosity, m^2/s
 ϕ = flow coefficient, $(Q/\pi\omega r_2 D_2 b_2)$
 ϕ_x, ϕ_y = phase angle in the stationary frame, rad
 φ = projection angle, rad
 ρ = density, kg/m^3
 τ, τ_w = shear stress, Wall shear stress, Pa
 ψ = head coefficient, $(gH/r_2^2\omega^2)$
 Ω = whirl rotational speed, rpm

ω = spin rotational speed, rpm
 ω_s = specific speed (metric), $(\omega Q^{1/2}/(gH)^{3/4})$

Subscripts

Cir = circular volute
Dif = diffuser
fsh = front shroud
Imp = impeller
Off = off-centered spinning
QS = quasi-steady model
Rad = radius-based volute
Rec = rectangular volute
Rnd = round asymmetric volute
Trn = transient model
Trp = trapezoidal volute
Vol = volute

References

- Childs, D. W., 2013, *Turbomachinery Rotordynamics With Case Studies*, Minter Spring, Wellborn, TX.
- API, 2002, "Axial and Centrifugal Compressors and Expander-Compressors for Petroleum, Chemical and Gas Industry Services," American Petroleum Institute, Washington, DC, Standard No. API 617.
- Ehrich, F. F., Spakovszky, Z. S., Martinez-Sanchez, M., Song, S. J., Wisler, D. C., Storage, A. F., Shin, H. W., and Beacher, B. F., 2001, "Unsteady Flow and Whirl-Inducing Forces in Axial-Flow Compressors—Part II: Analysis," *ASME J. Turbomach.*, **123**(3), pp. 446–452.
- Alford, J. S., 1965, "Protecting Turbomachinery From Self-Excited Rotor Whirl," *ASME J. Eng. Power*, **87**(4), pp. 333–344.
- Childs, D. W., 1989, "Fluid-Structure Interaction Forces at Pump-Impeller-Shroud Surfaces for Rotordynamic Calculations," *ASME J. Vib. Acoust.*, **111**(3), pp. 216–225.
- Untaroiu, A., Throckmorton, A. L., Patel, S. M., Wood, H. G., Allaire, P. E., and Olsen, D. B., 2005, "Numerical and Experimental Analysis of an Axial Flow Left Ventricular Assist Device: The Influence of the Diffuser on Overall Pump Performance," *Artif. Organs*, **29**(7), pp. 581–591.
- Suzuki, T., Prunieres, R., Horiguchi, H., Tsukiya, T., Taenaka, Y., and Tsujimoto, Y., 2007, "Measurements of Rotordynamic Forces on an Artificial Heart Pump Impeller," *ASME J. Fluids Eng.*, **129**(11), pp. 1422–1427.
- Chamieh, D. S., Acosta, A. J., Brennen, C. E., and Caughey, T. K., 1985, "Experimental Measurements of Hydrodynamic Radial Forces and Stiffness Matrices for a Centrifugal Pump Impeller," *ASME J. Fluids Eng.*, **107**(3), pp. 307–315.
- Ohashi, H., and Shoji, H., 1987, "Lateral Fluid Forces on Whirling Centrifugal Impeller (2nd Report: Experiment in Vaneless Diffuser)," *ASME J. Fluids Eng.*, **109**(2), pp. 100–106.
- Ehrich, F., 1993, "Rotor Whirl Forces Induced by the Tip Clearance Effect in Axial Flow Compressors," 14th Biennial ASME Design Technical Conference on Mechanical Vibration and Noise, Albuquerque, NM, Sept. 19–22, pp. 7–16.
- Williams, J. P., and Childs, D. W., 1991, "Influence of Impeller Shroud Forces on Turbopump Rotor Dynamics," *ASME J. Vib. Acoust.*, **113**(4), pp. 508–515.
- Adkins, D., and Brennen, C., 1988, "Analyses of Hydrodynamic Radial Forces on Centrifugal Pump Impellers," *ASME J. Fluids Eng.*, **110**(1), pp. 20–28.
- Tsujimoto, Y., Acosta, A. J., and Brennen, C. E., 1988, "Theoretical Study of Fluid Forces on a Centrifugal Impeller Rotating and Whirling in a Volute," *ASME J. Vib., Acoust., Stress, Reliab. Des.*, **110**(3), pp. 263–269.
- Childs, D. W., 1991, "Centrifugal-Acceleration Modes for Incompressible Fluid in the Leakage Annulus Between a Shrouded Pump Impeller and Its Housing," *ASME J. Vib. Acoust.*, **113**(2), pp. 209–218.
- Schobeiri, M. T., and Ghoreyshi, S. M., 2015, "The Ultrahigh Efficiency Gas Turbine Engine With Stator Internal Combustion," *ASME J. Eng. Gas Turbines Power*, **138**(2), p. 021506.
- Jafari, M. M., Atefi, G., Khalesi, J., and Soleymani, A., 2012, "A New Conjugate Heat Transfer Method to Analyze a 3D Steam Cooled Gas Turbine Blade With Temperature-Dependent Material Properties," *Proc. Inst. Mech. Eng., Part C*, **226**(5), pp. 1309–1320.
- Jafari, M. M., Atefi, G. A., and Khalesi, J., 2012, "Advances in Nonlinear Stress Analysis of a Steam Cooled Gas Turbine Blade," *Latin Am. Appl. Res.*, **42**(2), pp. 167–175.
- Baskharone, E. A., and Hensel, S. J., 1991, "A Finite-Element Perturbation Approach to Fluid/Rotor Interaction in Turbomachinery Elements—Part 2: Application," *ASME J. Fluids Eng.*, **113**(3), pp. 362–367.
- Moore, J. J., and Palazzolo, A. B., 2001, "Rotordynamic Force Prediction of Whirling Centrifugal Impeller Shroud Passages Using Computational Fluid Dynamic Techniques," *ASME J. Eng. Gas Turbines Power*, **123**(4), pp. 910–918.
- Moore, J. J., Ransom, D. L., and Viana, F., 2011, "Rotordynamic Force Prediction of Centrifugal Compressor Impellers Using Computational Fluid Dynamics," *ASME J. Eng. Gas Turbines Power*, **133**(4), p. 042504.
- Kim, E., and Palazzolo, A., 2016, "Rotordynamic Force Prediction of a Shrouded Centrifugal Pump Impeller-Part I: Numerical Analysis," *ASME J. Vib. Acoust.*, **138**(3), p. 031014.

- [22] Mortazavi, F., and Palazzolo, A., 2017, "Prediction of Rotordynamic Performance of Smooth Stator-Grooved Rotor Liquid Annular Seals Utilizing Computational Fluid Dynamics," *ASME J. Vib. Acoust.*, **140**(3), p. 031002.
- [23] Ohashi, H., Sakurai, A., and Nishihama, J., 1989, "Influence of Impeller and Diffuser Geometries on the Lateral Fluid Forces of Whirling Centrifugal Impeller," *NASA Lewis Research Center Rotordynamic Instability Problems in High-Performance Turbomachinery*, pp. 285–306.
- [24] Jery, B., 1987, "Experimental Study of Unsteady Hydrodynamic Force Matrices on Whirling Centrifugal Pump Impellers," *Ph.D. dissertation*, California Institute of Technology, Pasadena, CA.
- [25] Baskharone, E. A., and Hensel, S. J., 1991, "A Finite-Element Perturbation Approach to Fluid/Rotor Interaction in Turbomachinery Elements—Part I: Theory," *ASME J. Fluids Eng.*, **113**(3), pp. 353–361.
- [26] CFTurbo, 2017, "CFTurbo User Manual," CFTurbo GmbH, Dresden, Germany.
- [27] Jery, B., Brennen, C. E., Caughey, T. K., and Acosta, A., 1985, "Forces on Centrifugal Pump Impellers," *Second International Pump Symposium*, College Station, TX, pp. 21–32.
- [28] Gülich, J. F., 2008, *Centrifugal Pumps*, 2nd ed., Springer, Berlin.
- [29] Makay, E., and Barrett, J., 1984, "Changes in Hydraulic Component Geometries Greatly Increased Power Plant Availability and Reduced Maintenance Costs: Case Histories," *First International Pump Symposium*, pp. 85–100.
- [30] Bolleter, U., Wyss, A., Welte, I., and Stuerchler, R., 1987, "Measurement of Hydrodynamic Interaction Matrices of Boiler Feed Pump Impellers," *ASME J. Vib., Acoust., Stress, Reliab. Des.*, **109**(2), pp. 144–151.
- [31] Guelich, J. F., and Bolleter, U., 1992, "Pressure Pulsations in Centrifugal Pumps," *ASME J. Vib. Acoust.*, **114**(2), pp. 272–279.
- [32] ANSYS, 2017, "ANSYS User Manual," ANSYS Inc., Canonsburg, PA.
- [33] Ghoreyshi, S. M., and Schobeiri, M. T., 2017, "Numerical Simulation of the Multistage Ultra-High Efficiency Gas Turbine Engine, UHEGT," *ASME Paper No. GT2017-65029*.
- [34] Smirnov, P. E., and Menter, F. R., 2009, "Sensitization of the SST Turbulence Model to Rotation and Curvature by Applying the Spalart-Shur Correction Term," *ASME J. Turbomach.*, **131**(4), p. 041010.
- [35] Nikparto, A., and Schobeiri, M. T., 2018, "Combined Numerical and Experimental Investigations of Heat Transfer of a Highly Loaded Low-Pressure Turbine Blade Under Periodic Inlet Flow Condition," *Proc. Inst. Mech. Eng., Part A*, epub.
- [36] Untaroiu, A., Morgan, N., Hayrapetian, V., and Schiavello, B., 2017, "Dynamic Response Analysis of Balance Drum Labyrinth Seal Groove Geometries Optimized for Minimum Leakage," *ASME J. Vib. Acoust.*, **139**(2), p. 021014.
- [37] DaqiqShirazi, M., Torabi, R., Riasi, A., and Nourbakhsh, S., 2017, "The Effect of Wear Ring Clearance on Flow Field in the Impeller Sidewall Gap and Efficiency of a Low Specific Speed Centrifugal Pump," *Proc. Inst. Mech. Eng., Part C*, epub.
- [38] ANSYS, 2017, "ANSYS CFX-Solver Theory Guide," ANSYS Inc., Canonsburg, PA.
- [39] Pletcher, R. H., Tannehill, J. C., and Anderson, D., 2012, *Computational Fluid Mechanics and Heat Transfer*, 3rd ed., CRC Press, Boca Raton, FL.
- [40] Kim, E., and Palazzolo, A., 2016, "Rotordynamic Force Prediction of a Shrouded Centrifugal Pump Impeller—Part II: Stability Analysis," *ASME J. Vib. Acoust.*, **138**(3), p. 031015.
- [41] Franz, R., and Arndt, N., 1986, "Measurements of Hydrodynamic Forces on the Impeller of the HPOTP of the SSME," California Institute of Technology, Pasadena, CA, Report No. E249.2.
- [42] Ohashi, H., and Shoji, H., 1984, "Lateral Fluid Forces Acting on a Whirling Centrifugal Impeller in Vaneless and Vaned Diffuser," *NASA Lewis Research Center Rotordynamic Instability Problems in High-Performance Turbomachinery*, pp. 109–122.
- [43] Guinzburg, A., Brennen, C. E., Acosta, A. J., and Caughey, T. K., 1993, "The Effect of Inlet Swirl on the Rotordynamic Shroud Forces in a Centrifugal Pump," *ASME J. Eng. Gas Turbines Power*, **115**(2), pp. 287–293.
- [44] Mortazavi, F., Riasi, A., and Nourbakhsh, A., 2017, "Numerical Investigation of Back Vane Design and Its Impact on Pump Performance," *ASME J. Fluids Eng.*, **139**(12), pp. 121104–121109.
- [45] Shoji, H., and Ohashi, H., 1987, "Lateral Fluid Forces on Whirling Centrifugal Impeller (1st Report: Theory)," *ASME J. Fluids Eng.*, **109**(2), pp. 94–99.
- [46] Wachel, J. C., and Von Nimitz, W. W., 1981, "Ensuring the Reliability of Offshore Gas Compression Systems," *J. Pet. Technol.*, **33**(11), pp. 2252–2260.